Preparation and Characterization of Nanofibrous Perylene-Diimide−Polyelectrolyte Composite Thin Films

Thomas A. Everett, Amy A. Twite, Aifang Xie, Srinivas K. Battina, Duy H. Hua, and Daniel A. Higgins*

Department of Chemistry, Kansas State University, Manhattan, Kansas 66506

Received July 20, 2006. Revised Manuscript Received September 26, 2006

Composite nanofibrous thin films of a cationic, water-soluble perylene diimide and oppositely charged polyelectrolyte are prepared by sequential deposition from separate aqueous solutions of the two precursors. These materials may find future applications as semiconducting "wires" in organic electronics and photovoltaics. A new asymmetrically substituted perylene diimide (designated $C_{11}OPDI^+$) incorporating a hydrophobic ether tail is employed in their synthesis. Poly(acrylate) is used as the polyelectrolyte. Solution-phase and thin-film spectroscopic data show the composites form by binding and aggregation of $C_{11}OPDI^+$ to the polyelectrolyte. Tapping-mode AFM data show that the resulting nanofibers are tens of micrometers in length and are highly curved. Cross-sectional fiber size is shown to depend on the number of deposition cycles. Polarization-dependent fluorescence microscopy indicates the $C_{11}OPDI^+$ chromophores align perpendicular to the local long axis of the nanofibers. The $C_{11}OPDI^+$ molecules are concluded to form tail-to-tail parallel π-stacked structures that run along the fiber axis and are sandwiched between polyelectrolyte regions. In comparison to alternative methods, nanofiber formation is shown to be greatly enhanced when the composite is prepared by sequential deposition. A mechanism for enhanced fiber formation involving slow growth and solvent annealing of the composites is proposed.

Introduction

Perylenetetracarboxylic diimides (PDIs) have numerous potential applications in xerography,[1] organic electronics,[2] and solar energy conversion.[3] Contemporary research on PDIs usually involves the design and synthesis of new derivatives having enhanced solubility or unique modes of self-assembly. An important recent trend has been the development and implementation of water-soluble PDIs.[4] Water-soluble PDIs have been shown to exhibit lyotropic (chromonic) and thermotropic liquid crystallinity.[5−7] PDIs substituted at the bay positions have also been prepared and used in the self-assembly of novel composites that take advantage of both hydrogen bonding[8−10] and ionic intermolecular interactions.[7,8,11] Ionic interactions between oppositely charged PDIs have also been employed in layer-by-layer (LBL) self-assembly of pure PDI thin films[11] and composites.[12,13] The main purpose behind much of this work has been the optimization and control of materials organization. Improved organization may lead to the development of organic thin-film solar cells with enhanced energy conversion efficiencies and other unique properties, such as materials flexibility and the ability for self-repair.

For these same reasons, our group has recently undertaken the development and characterization of new PDI-based composite films formed by complexation of charged, water-soluble, asymmetrically substituted PDIs and oppositely charged polyelectrolytes.[14] The PDI−polyelectrolyte composites obtained are reminiscent of common polyelectrolyte−surfactant composites[15] and previously reported PDI−surfactant composites.[6,7] As in these other systems, self-assembly of the PDI−polyelectrolyte composites is a highly cooperative process and relies on electrostatic interactions between the polyelectrolyte and PDI along with $\pi-\pi$ and hydrophobic interactions of the PDIs themselves.

In an initial publication on these materials, we showed that composite films comprised of an asymmetrically substituted PDI ($C_{12}PDI^+$) and poly(acrylate) could be prepared by simply drop casting them from a single homogeneous solution of the two precursors.[14] The films obtained were comprised of semiordered, sub-micrometer-sized clusters that incorporated truncated PDI−polyelectrolyte bilayers. These

* Author to whom correspondence should be addressed. E-mail: higgins@ksu.edu.

(1) Law, K.-Y. *Chem. Rev.* **1993**, *93*, 449.
(2) Witte, G.; Woell, C. *J. Mater. Res.* **2004**, *19*, 1889.
(3) Gregg, B. A. *J. Phys. Chem. B* **2003**, *107*, 4688.
(4) Kohl, C.; Weil, T.; Qu, J.; Mullen, K. *Chem. Eur. J.* **2004**, *10*, 5297.
(5) Tam-Chang, S.-W.; Iverson, I. K.; Helbley, J. *Langmuir* **2004**, *20*, 342.
(6) Zakrevskyy, Y.; Faul, C. F. J.; Guan, Y.; Stumpe, J. *Adv. Funct. Mater.* **2004**, *14*, 835.
(7) Guan, Y.; Zakrevskyy, Y.; Stumpe, J.; Antonietti, M.; Faul, C. F. J. *Chem. Commun.* **2003**, 894.
(8) Würthner, F. *Chem. Commun.* **2004**, *2004*, 1564.
(9) Würthner, F.; Thalacker, C.; Sautter, A. *Adv. Mater.* **1999**, *11*, 754.
(10) Schenning, A. P. H. J.; Herrikhuyzen, J. V.; Jonkheijm, P.; Chen, Z.; Würthner, F.; Meijer, E. W. *J. Am. Chem. Soc.* **2002**, *124*, 10252.
(11) Tang, T.; Qu, J.; Mullen, K.; Webber, S. E. *Langmuir* **2006**, *22*, 26.
(12) Martinson, A. B. F.; Massari, A. M.; Lee, S. J.; Gurney, R. W.; Splan, K. E.; Hupp, J. T.; Nguyen, S. T. *J. Echem. Soc.* **2006**, *153*, A527.
(13) Marcon, R. O.; dos Santos, J. G.; Figueiredo, K. M.; Brochsztain, S. *Langmuir* **2006**, *22*, 1680.
(14) Xie, A.; Liu, B.; Hall, J. E.; Barron, S. L.; Higgins, D. A. *Langmuir* **2005**, *21*, 4149.
(15) Zhou, S.; Chu, B. *Adv. Mater.* **2000**, *12*, 545.

10.1021/cm061695r CCC: $33.50
Published on Web 11/17/2006

Scheme 1. Structure of the Perylene Diimide ($C_{11}OPDI^+$) Employed and the Poly(acrylate) Monomer (PA^-)

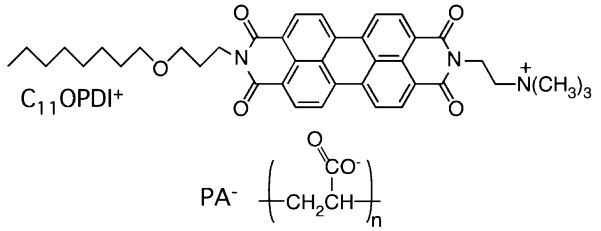

films exhibited diodelike behavior when included in rudimentary p−n heterojunction devices and yielded measurable photovoltages when exposed to visible light.[14] Unfortunately, film discontinuity appeared to limit exciton hopping and electrical conductivity. In addition, $C_{12}PDI^+$ was of limited solubility (≈100 μM solutions could be obtained). To overcome these limitations, we have since developed new PDIs that exhibit better water solubility. We have also begun to explore alternative film deposition procedures that may lead to films of better or alternative morphologies.

Here, we demonstrate the use of sequential deposition methods as a means to prepare PDI−polyelectrolyte composite thin films comprised of curved nanofibers. The resulting materials are characterized using several spectroscopic and microscopic methods. A new asymmetrically substituted PDI (designated $C_{11}OPDI^+$) is employed, while poly(acrylate) (PA^-) is again used as the polyelectrolyte. The structures of $C_{11}OPDI^+$ and PA^- are given in Scheme 1. A long-chain ether was incorporated as one of the imide substituents in $C_{11}OPDI^+$ to help improve solubility.[16] Sequential deposition was chosen on the expectation that repeatedly dipping the films into separate solutions of the two components would result in effective solvent annealing of the materials as they were deposited. In addition, relatively slow growth of the composites during sequential deposition was expected to yield films comprised of larger domains of ordered structures.

While the sequential deposition process employed herein is similar to well-known LBL deposition,[11−13] the film structures obtained differ dramatically from the usual layered architectures (i.e., nanofibers are formed). While nanofibrous PDI-based structures have been reported previously for both pure PDI systems[8,11,17−21] and other composites,[6−8] formation and deposition of the fibers described herein is dramatically enhanced by incorporation of the polyelectrolyte. Nanofiber formation in these materials results from binding and aggregation of $C_{11}OPDI^+$ along the polyelectrolyte backbone. In the future, these nanofibers may find applications as semiconducting wires[10,18,19] in organic electronics and photovoltaics. Important advantages of these materials over existing alternatives include the ability to cast them on arbitrary substrates from aqueous solution and the potential for increased material strength because of binding of $C_{11}OPDI^+$ to the polyelectrolyte.

Experimental Section

Synthesis of *N*-(3(Octyloxy)propyl)-*N*′(2-(trimethylammonio)ethyl)perylene-3,4,9,10-tetracarboxylic Diimide Iodide ($C_{11}OPDI^+ \cdot I^-$). Unless otherwise noted, all starting materials were obtained from Aldrich and were used as received. Discussion of this synthesis is broken down into separate procedures used in the preparation of each precursor.

Preparation of 3-(Octyloxy)propanenitrile.[16] A mixture of 4.0 g (76 mmol) acrylonitrile, 4.4 g (34 mmol) 1-octanol, and 0.05 g (0.9 mmol) dry sodium methoxide was prepared in a nitrogen-purged flask. The reaction mixture was left stirring under positive nitrogen pressure for 24 h. Acetic acid (0.2 mL) was subsequently added, and unreacted acrylonitrile was removed on a rotary evaporator. The product was collected by adding 25 mL of water to the flask, followed by extraction into four 25-mL portions of chloroform. The chloroform solution was dried over sodium sulfate, and the faint yellow liquid product was collected by rotary evaporation. After further drying on a vacuum line, 3.8 g (62% yield) of the product was obtained. NMR spectra showed the product to be of high purity. ^{1}H NMR (400 MHz, $CDCl_3$) δ 3.64 (t, 2 H, CH_2O), 3.48 (t, 2 H, CH_2O), 2.57 (t, 2 H, CH_2CN), 1.58 (pent, 2 H, CH_2), 1.28 (bs, 10 H, CH_2), 0.88 (t, 3 H, CH_3) ppm.

Preparation of 3-(Octyloxy)propanamine. To a solution of 5.0 g (27 mmol) 3-(octyloxy)propanenitrile in 20 mL of ethanol (distilled over magnesium) was added 0.2 g (0.9 mmol) platinum oxide. The mixture was placed in a hydrogenator and was shaken under 30 psi hydrogen gas at room temperature for 1 day. Afterward, the mixture was diluted with ethanol, filtered through a layer of Celite, and concentrated to give 4.9 g (96% yield) of 3-(octyloxy)propanamine. The product was used without further purification. ^{1}H NMR (400 MHz, $CDCl_3$) δ 3.47 (t, 2 H, CH_2O), 3.39 (t, 2 H, CH_2O), 2.72 (t, 2 H, CH_2N), 1.85 (bs, 2 H, NH_2), 1.78 (pent, 2 H, CH_2), 1.56 (pent, 2 H, CH_2), 1.28 (bs, 10 H, CH_2), 0.88 (t, 3 H, CH_3) ppm; ^{13}C NMR (100 MHz, $CDCl_3$) δ 71.3 (t, CH_2O), 69.6 (t, CH_2O), 47.6 (t, CH_2N), 32.0 (t), 30.1 (t), 30.0 (t), 29.7 (t), 29.5 (t), 26.4 (t), 22.9 (t), 14.3 (q, CH_3) ppm; MS (electrospray CI) *m*/*z* 188.02 (M+1).

Preparation of N-(3-(Octyloxy)propyl)-N′(2-(N,N-dimethylamino)ethyl)perylene-3,4,9,10-tetracarboxylic Diimide. A one-pot procedure was employed in this synthesis. To a 300-mL round-bottom flask were added 300 mg (0.75 mmol) perylene tetracarboxylic dianhydride, 450 mg (2.4 mmol) 3-(octyloxy)propanamine, 67.6 mg (0.77 mmol) *N*,*N*-dimethylethylenediamine, and 200 mL of pyridine. The reaction mixture was refluxed and stirred under a nitrogen atmosphere for ≈24 h. The pyridine was subsequently removed on a rotary evaporator. The resulting solids were rinsed with three 25-mL portions of cold ethanol, were collected by vacuum filtration, and were dried under vacuum overnight. The crude product was a mixture of two symmetrically substituted perylene diimides and the desired asymmetrically substituted compound. The asymmetric compound was obtained in high purity as the middle band on a silica gel column, using a mixture of chloroform, ethanol, and triethylamine (20:1:0.1) as the eluent. After drying under vacuum, 110 mg (22% yield) of the desired product was obtained. ^{1}H NMR (400 MHz, $CDCl_3$) δ 8.6 (m, 8 H, perylene), 4.36 (m, 4 H, diimide CH_2N), 3.59 (t, 2 H, CH_2O), 3.40 (t, 2 H, CH_2O), 2.72 (t, 2 H, CH_2N), 2.39 (s, 6 H, $(CH_3)_2N$), 2.05 (pent, 2

(16) Cormier, R. A.; Gregg, B. A. *Chem. Mater.* **1998**, *10*, 1309.
(17) Würthner, F.; Chen, Z.; Dehm, V.; Stepanenko, V. *Chem. Commun.* **2006**, 1188.
(18) Balakrishnan, K.; Datar, A.; Oitker, R.; Chen, H.; Zuo, J.; Zang, L. *J. Am. Chem. Soc.* **2005**, *127*, 10496.
(19) Balakrishnan, K.; Datar, A.; Naddo, T.; Huang, J.; Oitker, R.; Yen, M.; Zhao, J.; Zang, L. *J. Am. Chem. Soc.* **2006**, *128*, 7390.
(20) Datar, A.; Balakrishnan, K.; Yang, X.; Zuo, X.; Huang, J.; Oitker, R.; Yen, M.; Zhao, J.; Tiede, D. M.; Zang, L. *J. Phys. Chem. B* **2006**, *110*, 12327.
(21) Herrikhuyzen, J. V.; Syamakumari, A.; Schenning, A. P. H. J.; Meijer, E. W. *J. Am. Chem. Soc.* **2004**, *126*, 10021.

H, CH_2), 1.45 (pent, 2 H, CH_2) 1.20 (bs, 10 H, CH_2), 0.82 (t, 3 H, CH_3) ppm. ^{13}C NMR (100 MHz, $CDCl_3$) δ 163.5 (4 C, C═O), 134.5 (4 C), 131.5 (4 C), 131.4 (4 C), 123.5 (2 C), 123.4 (2 C), 123.1 (2 C), 71.2, 69.1, 57.2, 46.0 (2 C), 38.6, 32.0, 30.0, 29.7, 29.5, 2.4, 26.4, 22.8, 14.4 ppm. MS (MALDI) *m*/*z* 632.37 (M + 1).

Preparation of the Title Compound ($C_{11}OPDI^+ \cdot I^-$), MW = 773.6 g/mol (See Scheme 1). To a 100 mL-round-bottom flask containing a stir bar and 50 mL of chloroform were added 100 mg (0.16 mmol) *N*-(3-(octyloxy)propyl)-*N*′(2-(*N*,*N*-dimethylamino)ethyl)perylene-3,4,9,10-tetracarboxylic diimide and 100 μL (1.6 mmol) of iodomethane. The reaction mixture was refluxed overnight under a nitrogen atmosphere. $C_{11}OPDI^+ \cdot I^-$ precipitated from solution as the reaction proceeded. Chloroform and excess iodomethane were removed on a rotary evaporator. The product was suspended and washed in three portions of ethanol and was collected by centrifugation. The final product was obtained in good yield after drying overnight in a vacuum oven at 50 °C. MS, (MALDI) *m*/*z* 646.27 (M^+; without iodide); calculated *m*/*z* for $C_{40}H_{44}N_3O_5^+$: 646.33 (100%). The mass spectrum indicated the sample was of good purity.

Deposition of $C_{11}OPDI^+ \cdot PA^-$ Composite Films. $C_{11}OPDI^+$ and PA^- were deposited on clean glass microscope coverslips by sequentially dipping them into (1) a 270 μM aqueous solution of $C_{11}OPDI^+$ (1-min dip), (2) deionized water (30-s dip), (3) a 2.43 mM (pH = 7, unbuffered) aqueous solution of sodium PA^- (concentration based on monomer, 1-min dip), and (4) deionized water (30-s dip). A withdrawal rate of 2 mm/s was used in each case. This sequence was repeated up to 55 times during deposition of thin-film samples. Prior to use, the microscope coverslips had been cleaned by exposing them to an air plasma for 5 min.

All solutions were prepared using 18 MΩ·cm water. $C_{11}OPDI^+$ solutions were prepared by first dissolving the compound in methanol. An equal volume of water was then added and the solution was brought to a boil. After evaporation of the methanol, the remaining aqueous solution was transferred to a volumetric flask, allowed to cool, and subsequently diluted to the mark with water.

Characterization of $C_{11}OPDI^+ \cdot PA^-$ Composite Films. Thin-film and solution-phase fluorescence spectra of $C_{11}OPDI^+$ and its complex with PA^- were obtained using a SPEX Fluoromax-2 fluorimeter. Absorption spectra were obtained on an HP-8453 diode array spectrometer. A clean coverslip was used as the reference in thin-film absorption spectra.

Composite thin-film morphology was characterized by tapping-mode AFM, using a Digital Instruments Multimode AFM. Molecular organization in the films was characterized using polarization-dependent confocal fluorescence microscopy. A home-built sample scanning confocal microscope that has been described previously was used.[22] Briefly, the sample being imaged sits on top of a closed loop piezoelectric scanning stage (±3 nm reproducibility) that is mounted on an inverted epi-illumination microscope (Nikon). Light at 514 nm from an argon ion laser (Coherent) was used to excite the sample. This light was delivered to the microscope via a single-mode optical fiber. Prior to entering the microscope, the laser light was first directed through polarization optics for control of both the incident power and polarization state. The light was then directed into the back aperture of a high numerical aperture (NA = 1.3) oil immersion objective by reflection from a dichroic mirror. The objective produced a diffraction-limited focused spot of light in the sample. Typical average incident powers used were ≈200 nW. Fluorescence from the sample was collected using the same objective and was subsequently directed into the detection path.

(22) Hou, Y.; Bardo, A. M.; Martinez, C.; Higgins, D. A. *J. Phys. Chem. B* **2000**, *104*, 212.

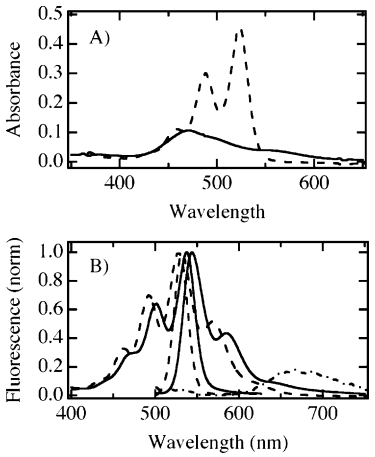

Figure 1. (A) UV−vis spectra of 10 μM $C_{11}OPDI^+$ in aqueous solution (—) and in methanol (-----). (B) Normalized fluorescence excitation (monitoring 650 nm) and emission spectra (exciting at 488 nm) of 10 μM $C_{11}OPDI^+$ in aqueous solution (—) and in methanol (-----). Also shown is the emission spectrum of 10 μM $C_{11}OPDI^+$ in the presence of 20 μM PA^- (-•-•-•-). Fluorescence emission from $C_{11}OPDI^+$ in water is ≈21 times weaker than in methanol. Emission from the $C_{11}OPDI^+ \cdot PA^-$ complex is ≈100 times weaker than from $C_{11}OPDI^+$ in methanol. Aqueous $C_{11}OPDI^+$ and $C_{11}OPDI^+ \cdot PA^-$ emission spectra are plotted on the same scale.

Residual excitation light was removed with appropriate notch (Kaiser Optical) and bandpass (Chroma Technologies) filters. A single-photon-counting avalanche photodiode (Perkin-Elmer) was employed as the detector. In polarization-dependent studies, the incident polarization was alternately set parallel and perpendicular to the scan direction by use of a 514-nm halfwave plate (Special Optics). Total fluorescence (i.e., all polarizations) was detected.

Results and Discussion

Bulk Solution-Phase Spectroscopy. Solution-phase spectroscopic studies were performed to determine the form (i.e., monomer or aggregate) of $C_{11}OPDI^+$ present in aqueous solution and, hence, to better understand its deposition mechanism. $C_{11}OPDI^+ \cdot I^-$ is reasonably soluble in water, with concentrations as high as 0.3 mM readily prepared in the absence of electrolytes. Figure 1 depicts several absorption and fluorescence spectra obtained from dilute (i.e., 10 μM) solutions. Absorption spectra recorded for aqueous solutions (see Figure 1A) are significantly broadened and blue-shifted from the monomer spectrum, indicating $C_{11}OPDI^+$ is present in an aggregated form (i.e., similar to a H-aggregate). The monomeric form of $C_{11}OPDI^+$ is observed in methanolic solution at this same concentration. The monomer spectrum in methanol appears as a simple vibronic progression, with an origin at 522 nm (Figure 1A).

In contrast to the absorption spectrum of aqueous $C_{11}OPDI^+$, the fluorescence excitation and emission spectra obtained at the same 10 μM concentration are clearly those of the monomer. Figure 1B shows representative fluorescence spectra obtained in water and methanol. Aside from a slight solvent-dependent shift, and a change in emission intensity, both aqueous and methanolic solutions yield mirror-image spectra that appear as simple vibronic progressions. These results indicate that essentially all fluorescence from aqueous solutions comes from a small amount of monomeric $C_{11}OPDI^+$. The fact that the fluorescence excitation and absorption spectra are so dramatically different indicates that the aggregates formed by $C_{11}OPDI^+$ alone are nonfluorescent.

While the $C_{11}OPDI^+$ fluorescence spectra in water and methanol are qualitatively similar in appearance, the difference in emission intensities from these two solutions is profound. The fluorescence obtained from an aqueous 10 μM solution of $C_{11}OPDI^+$ is ≈5% of that from an equivalent methanolic solution. Neglecting any difference in fluorescence quantum yields for monomeric $C_{11}OPDI^+$ in methanol and water, the monomer appears to comprise <10% of the species present in 10 μM aqueous solutions. It is therefore concluded that $C_{11}OPDI^+$ is present predominantly in an aggregated form at the much higher concentrations used in thin-film deposition, as described below.

Also shown in Figure 1B is the emission spectrum for a $C_{11}OPDI^+ \cdot PA^-$ complex in aqueous solution. Unlike the aggregates formed in the absence of polyelectrolyte, the $C_{11}OPDI^+ \cdot PA^-$ complex is somewhat fluorescent. Emission from this sample falls predominantly in a broad, featureless, excimer-like emission band centered at ≈670 nm. Emission in this region is observed only for superstoichiometric complexes and is approximately 5-fold weaker than the monomer emission obtained in aqueous solution in the absence of PA^- (both aqueous emission spectra shown in Figure 1B are plotted on the same scale). These observations suggest the PDI chromophores take on a tightly π-stacked structure in the absence of polyelectrolyte and in substoichiometric complexes. In superstoichiometric complexes, the $C_{11}OPDI^+$ clearly forms a different type of aggregate, perhaps with greater chromophore spacing and mobility, as controlled by the polyelectrolyte. In this latter case, the chromophores assume a geometry that allows for excimer formation. In the former, emission must be forbidden by the symmetry properties of the aggregate. Subtle changes in the π-stacking of PDI chromophores have been shown previously to lead to dramatic changes in their spectroscopic properties.[23,24]

Sequential Deposition of Composite Films. Deposition of $C_{11}OPDI^+ \cdot PA^-$ composite thin films was accomplished by sequentially dipping a clean microscope coverslip into four separate solutions (aqueous $C_{11}OPDI^+$, water, aqueous PA^-, and water) as defined in the Experimental Section. The same strong polyelectrolyte binding and aggregation processes active in the solution-phase studies described above are also expected to occur during sequential deposition.

Figure 2A presents representative thin-film absorption spectra obtained after different numbers of deposition cycles. Here, a single deposition cycle involves dipping a coverslip sequentially into all four solutions listed above. Figure 2B depicts a representative bulk fluorescence spectrum obtained from these same films. Both the peak absorbance and emission intensity from the films increase with the number of deposition cycles. However, the shapes and positions of the spectra show only very subtle changes over the full range of deposition cycles employed (from 1 to 55). Hence, it may be concluded that while the amount of material deposited increases with the number of deposition cycles, the structure of the aggregated composite materials remains relatively unchanged.

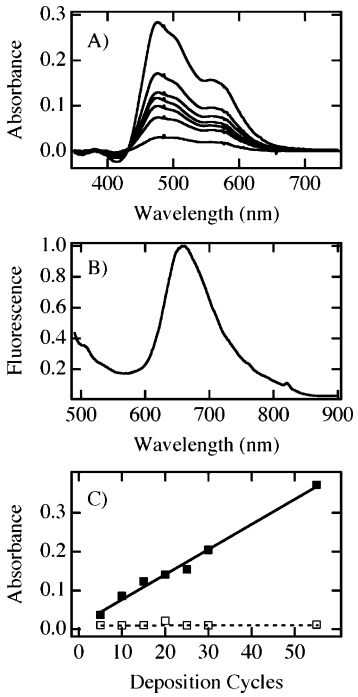

Figure 2. (A) UV−vis spectra (corrected for scattering) from $C_{11}OPDI^+ \cdot PA^-$ composite films as a function of the number of deposition cycles. The spectra shown are for 5, 10, 15, 20, 25, 30, and 55 cycles (increasing absorbance). (B) Fluorescence spectrum from a composite film deposited in 20 cycles. (C) Peak absorbance at 480 nm taken from A as a function of the number of deposition cycles. Data obtained for both the composite (filled squares) and in the absence of PA^- (open squares) are shown.

The aggregates formed in the composite thin films are similar to, but somewhat different from, those found in 10 μM aqueous solution. Notably, the thin-film absorption spectra have a slightly more pronounced shoulder at 560 nm. Likewise, the excimer-like emission observed from the thin films is slightly blue-shifted from that observed in solution (660 nm vs 670 nm). Although the exact structural differences in the film and solution aggregates are not known, subtle changes in PDI packing are likely involved.[23,24]

The thin-film absorption spectra (Figure 2A) show a monotonic increase in absorbance with the number of deposition cycles. Figure 2C plots the peak absorbance (at 480 nm) observed (filled squares). This plot is surprisingly linear, given the film morphology depicted below. A slope of 0.005 absorbance units per dipping cycle is obtained, indicating that facile deposition of $C_{11}OPDI^+$ occurs in the presence of PA^-. In contrast, relatively little material is deposited in the absence of the polyelectrolyte. Absorbance data obtained as a function of the number of dipping cycles in this case are also plotted in Figure 2C (open squares). As is readily apparent, the slope of the plot obtained in the absence of PA^- is dramatically smaller than that for the composite. It is concluded that PA^- is necessary for efficient deposition of the thin films prepared herein and that PA^- is an integral component of the nanofibrous structures described below. These results also indicate that composite deposition proceeds in a fashion similar to traditional LBL methods, in which a reversal of surface charge occurs after the substrate is dipped in each precursor solution (i.e., $C_{11}OPDI^+$or PA^-).

(23) Klebe, G.; Graser, F.; Hädicke, E.; Berndt, J. *Acta Crystallogr.* **1989**, *B45*, 69.
(24) Kazmaier, P. M.; Hoffmann, R. *J. Am. Chem. Soc.* **1994**, *116*, 9684.

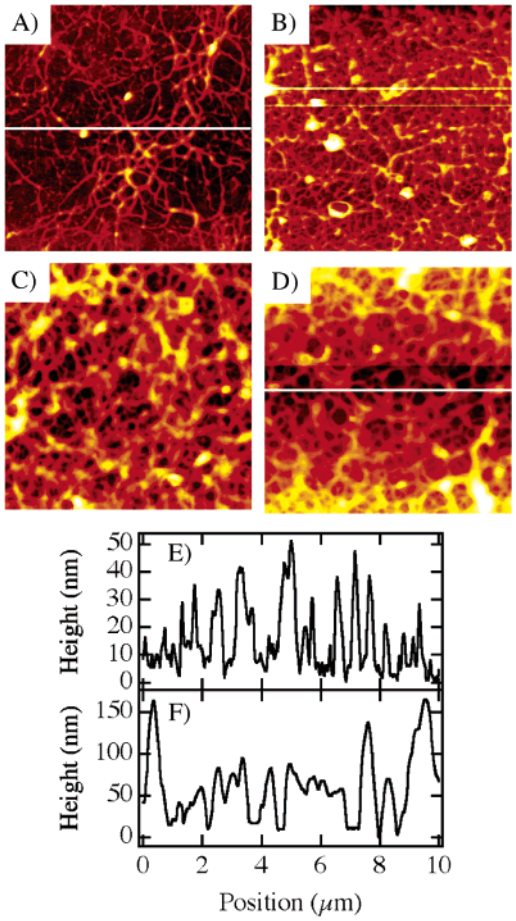

Figure 3. Tapping-mode AFM images of films prepared using (A) 5, (B) 10, (C) 20, and (D) 30 deposition cycles. Each image is of a 10 × 10 μm^2 region. (E) and (F) Line profiles taken across the images in A and D, providing information on feature height and width.

Composite Film Morphology. Tapping-mode AFM images of the sequentially deposited films show that they are highly nonuniform and are comprised of novel curved nanofibers. Representative images of films obtained after 5, 10, 20, and 30 deposition cycles are shown in Figure 3. Images of samples recorded at earlier stages in the deposition process (i.e., after one cycle) show numerous small features (likely fiber nucleation sites) and a few small, straight, needlelike fibers. While related nanofibers have been observed previously in films deposited from pure PDIs,[8,11,17−21] and in PDI−surfactant composites,[6,7] to our knowledge, nanofibrous PDI−polyelectrolyte composites have never before been reported.

The nanofibers of the $C_{11}OPDI^+ \cdot PA^-$ composite films are generally observed to be several micrometers to tens of micrometers in length. Their cross-sectional dimensions increase with the number of deposition cycles employed. Qualitative data on this trend may be found in the line profiles plotted in Figure 3E and F in which both fiber height and width are shown to increase. Observation of the nanofibrous morphology is independent of the amount of material deposited, however, up to the maximum number of deposition cycles studied (i.e., 55).

As with $C_{11}OPDI^+$ deposition, formation of the nanofibers is greatly enhanced in the presence of PA^-. Figure 4 shows an AFM image acquired for $C_{11}OPDI^+$ deposited in 30 cycles, without PA^-. Similar images are obtained after only a single deposition of $C_{11}OPDI^+$. The amount of material deposited (after more than one cycle) is clearly much smaller than is observed for the composite (as is consistent with the UV−vis data presented above). More importantly, very few nanofibers are observed in AFM images of films deposited without PA^-. Furthermore, those that are present appear predominantly as small, straight, needlelike fibers, reminiscent of those observed previously for other pure PDI materials.[8,11,17−21] This result provides direct support for the conclusion that PA^- is an integral component of the fibers and that it plays a central role in determining the nanofibrous morphology of these composites.

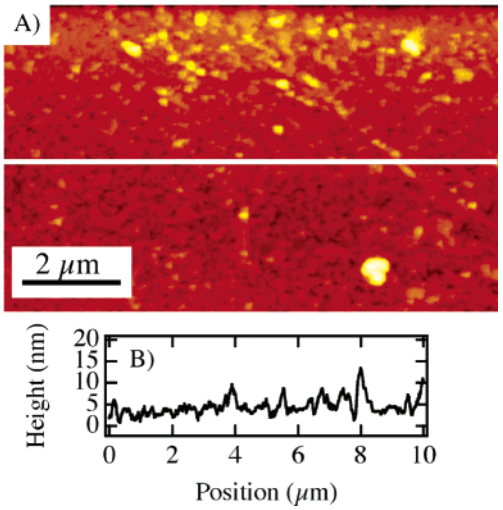

Figure 4. (A) Tapping-mode AFM image of $C_{11}OPDI^+$ film deposited without the use of PA^- in 30 deposition cycles. (B) Line profile taken across this image, showing feature height and width.

The observation of nanofibers also depends on the exact method and conditions employed for materials deposition. $C_{11}OPDI^+ \cdot PA^-$ composites drop cast from a single, homogeneous solution of the two precursors yield films of nanoclusters, not nanofibers. Film morphology in this case is identical to that observed in our previous studies of related drop-cast $C_{12}PDI^+ \cdot PA^-$ composites.[14] Nanofiber size and film morphology is believed to depend on rate of fiber growth and therefore varies with concentration, temperature, ionic strength, and solution pH. These effects will be explored in future investigations.

Nanofiber Size. As noted above, the size of the $C_{11}OPDI^+ \cdot PA^-$ nanofibers increases with the number of deposition cycles. Quantitative data on nanofiber size were obtained by performing autocorrelations of the AFM images[25,26] along two dimensions, as defined in eq 1

$$C(\xi) = \frac{\langle h(x+\xi)h(x)\rangle}{\langle h(x)^2\rangle} \quad (1)$$

Here, $h(x)$ represents the topographic height (i.e., a line profile) along either the horizontal or vertical directions, and $C(\xi)$ is the resulting autocorrelation. The brackets in eq 1

(25) Petersen, N. O.; Höddelius, P. L.; Wiseman, P. W.; Seger, O.; Magnusson, K.-E. *Biophys. J.* **1993**, *65*, 1135.
(26) Suzuki, A.; Yamazaki, M.; Kobiki, Y.; Suzuki, H. *Macromolecules* **1997**, *30*, 2350.

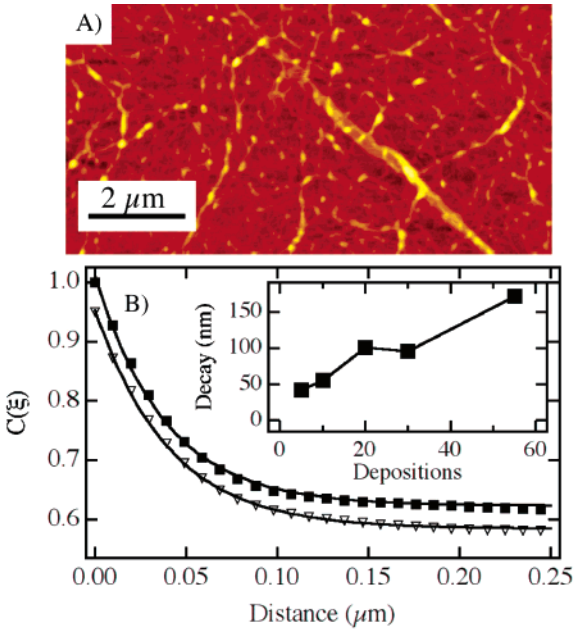

Figure 5. (A) Tapping-mode AFM image of a sample prepared using five deposition cycles. (B) Autocorrelation functions derived from the image in A along the horizontal (solid squares) and vertical (open triangles) directions in the image. The vertical autocorrelation data has been offset along the *y*-direction to aid in visualization. Inset: characteristic nanofiber size as a function of deposition cycles.

indicate that a spatial average is taken. Figure 5A depicts a subsection of a tapping-mode AFM image obtained from a film deposited in five cycles. Figure 5B depicts the autocorrelations obtained from this image. These autocorrelations actually represent the average autocorrelations obtained from all 512 vertical and horizontal line profiles comprising the image.

The distance over which each autocorrelation function decays provides a measure of nominal nanofiber size. Since only short-range information can be extracted from such autocorrelations (i.e., insufficient information on sample features that are large relative to the image size exists), the information obtained is actually proportional to the average nanofiber cross-sectional size. Both height and width information are included in this data in part because of convolution of the AFM probe shape with sample features of different heights. In addition, the autocorrelation decays are broadened by the random orientations of the nanofibers. While it is not possible to present an exact model for the mathematical form of the autocorrelation decays under these circumstances, they are observed to fit well to single exponentials (see Figure 5B). The inset shown in Figure 5B plots the average feature size (i.e., the exponential decay constant) observed for different numbers of deposition cycles. As is clearly apparent from these data, nanofiber size increases with the number of cycles.

The rate at which the fibers grow with the number of deposition cycles is also important. Initially, fiber size increases rapidly from zero to an average of 40 nm when as few as five deposition cycles are employed. The fiber growth rate appears to decrease as more material is deposited, although film thickness continues to increase. This can be readily explained by noting that as the fibers grow, the gaps between individual fibers fill in to form a continuous film.

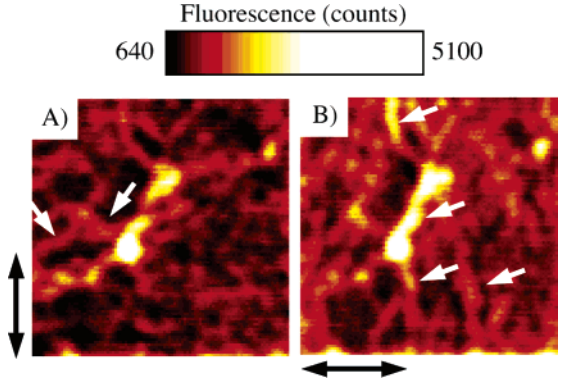

Figure 6. (A) and (B) Polarization-dependent confocal fluorescence microscopy images ($10 \times 10\ \mu m^2$) of $C_{11}OPDI^+ \cdot PA^-$ films recorded under the incident polarizations designated by the appended black arrows. The white arrows point to representative polarization-dependent features in the images. This sample was prepared in 10 deposition cycles.

At the same time, new fibers also nucleate and grow, leading to a sort of steady-state nanofiber size for relatively thick films.

Chromophore Alignment and Fiber Structure. Chromophore organization within the composite nanofibers was probed by polarization-dependent confocal fluorescence microscopy. Figure 6 depicts two representative fluorescence images of the same sample region, excited with polarized 514-nm light. The two images shown were recorded under orthogonal incident polarization conditions, as designated by the appended double-ended arrows. Total fluorescence was detected (i.e., no analyzer was used). Two important factors complicate these experiments. First, the fibers are only weakly fluorescent (the fluorescence quantum yield of the composite is ≈100 times smaller than that of the monomer in methanol solution). Second, the fluorescence emission from the fibers clearly varies with their thickness. Nevertheless, these data show that most efficient fluorescence excitation occurs when the incident polarization is oriented approximately perpendicular to the (local) long axis of the individual nanofibers. Since the lowest energy electronic transition in PDI-based chromophores is known to be polarized along the long axis of the molecule (i.e., along the axis running between the imide moieties),[24,27,28] it may be concluded that the PDI chromophores are stacked with their conjugated ring planes oriented approximately perpendicular to the local nanofiber axis. This same alignment has been observed previously in other PDI-based nanofibrous materials.[20]

Figure 7 shows a model for the proposed organization of the composite nanofibers. In this model, the fibers are comprised of parallel rows of $C_{11}OPDI^+$ π-stacks in which the chromophores take on a H-aggregate-like organization, having only a small lateral offset in the chromophore positions within the individual π-stacks. The $C_{11}OPDI^+$ rows are separated by their interdigitated ether tails, forming a nonpolar region sandwiched between aromatic domains. The charged headgroups of $C_{11}OPDI^+$ and the polyelectrolyte

(27) Adachi, M.; Murata, Y.; Nakamura, S. *J. Phys. Chem.* **1995**, *99*, 14240.
(28) Struijk, C. W.; Sieval, A. B.; Dakhorst, J. E. J.; van Dijk, M.; Kimkes, P.; Koehorst, R. B. M.; Donker, H.; Schaafsma, T. J.; Picken, S. J.; van de Craats, A. M.; Warman, J. M.; Zuilhof, H.; Sudhölter, E. J. R. *J. Am. Chem. Soc.* **2000**, *122*, 11057.

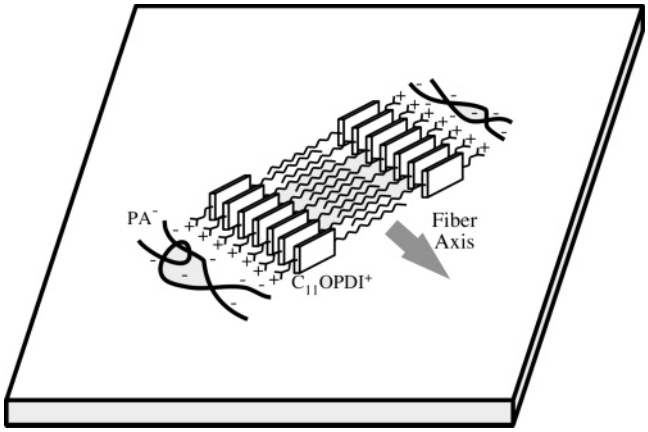

Figure 7. Model for $C_{11}OPDI^{+}$·PA^{-} organization in short segments of the composite nanofibers.

then form highly ionic regions on the outsides of the fibers. The highly curved fibers are actually believed to incorporate short segments of the structures depicted in Figure 7. Disruption of this structure allows for the fibers to bend, as observed in images of these materials.

Alternative organizational models for the fibers may also be proposed. For example, they may also result from formation of columnar stacks of $C_{11}OPDI^{+}$ surrounded by polyelectrolyte.[17] At the present time, the available data do not allow for a distinction to be made between these two models and either may be correct. The parallel π-stack organization proposed here was selected as being most likely because it allows for most parallel stacking of the PDI chromophores.

Fiber Growth Mechanism. The differences in film morphology observed for the materials deposited sequentially and from homogeneous mixtures provide important clues as to the fiber growth mechanism. Again, sequential deposition of $C_{11}OPDI^{+}$ and PA^{-} from separate aqueous solutions appears to greatly enhance nanofiber formation. Fiber growth in sequentially deposited composites is attributed in part to the solvent annealing that likely occurs during deposition. The mostly insoluble surface-bound composites may slowly rearrange to form fibrous structures as they are repeatedly dipped into the various solutions. It is also very likely that slow growth of the composites aids fiber formation. During sequential deposition, only a small amount of material is deposited in each dipping step. Some material is also removed during subsequent rinsing. As a result, composite formation is relatively slow and somewhat like a slow crystallization in which larger, more uniformly organized structures can grow. Fibers are not prevalent in films drop cast from homogeneous aqueous solution because the complexes form extremely rapidly. Short aggregated structures result in this case. Finally, it is also very clear that different aggregate morphologies and polymer conformations exist in the aqueous solutions used in sequential deposition. The polymer in homogeneous aqueous solution (in the presence of $C_{11}OPDI^{+}$) likely takes on a collapsed conformation, surrounding short segments of $C_{11}OPDI^{+}$ aggregates. By itself, PA^{-} would take on a relatively more extended conformation. The binding of extended (rather than collapsed) PA^{-} strands could also aid in nanofiber growth. For its part, the $C_{11}OPDI^{+}$ likely forms short, needlelike fibers in solution with or without the polyelectrolyte. This conclusion is supported by AFM images of the composites at early stages of deposition (i.e., absent PA^{-} or after one deposition cycle). During sequential deposition, these short fibers likely bind to the pre-existing PA^{-} film and behave as templates or nucleation sites for continued fiber growth in future deposition cycles.

Conclusions

In summary, sequential deposition of nanofibrous perylene-diimide−polyelectrolyte composites from aqueous solutions has been demonstrated. The films prepared incorporate long, curved, composite nanofibers, as observed by AFM and optical microscopy. Film growth and nanofiber formation is greatly enhanced by incorporation of the polyelectrolyte. Such fibers are not readily observed in drop-cast films of the same materials, indicating that sequential deposition also enhances fiber formation. It is believed that nanofiber formation results from solvent-annealing and slow-growth effects that occur when short aggregated PDI segments and extended polyelectrolyte strands are sequentially deposited. Polarization-dependent fluorescence imaging indicates that the chromophores in the fibers are oriented perpendicular to the long fiber axis. It is concluded that the fibers are comprised of parallel π-stacked $C_{11}OPDI^{+}$ assemblies sandwiched between polyelectrolyte regions. The nanofibers obtained are expected to behave as semiconducting wires with possible applications in large-area, flexible, organic photovoltaic thin films. These composites have several advantages over existing alternatives, including the fact that they are deposited from aqueous solutions and that incorporation of the polyelectrolyte is expected to increase the mechanical strength of the resulting materials.

Acknowledgment. The authors are grateful to the National Science Foundation (DMR-0076169, CHE-0404578, and CHE-0555341), the Office of Naval Research (N00014-02-1-0584), American Chemical Society PRF (40345-AC1), and the National Institutes of Health (AG025500) for support. Christer Aakeröy and Takashi Ito are thanked for helpful discussions on these materials. Richard and Stuart Bachamp and James Hodgson are thanked for their help in constructing the dip coater.

CM061695R